Revealing the Evolution and Small-Scale Variability of the Morning Transition Phase in the atmospheric boundary layer using Distributed Temperature Sensing

Antonia M Fritz[1,1], Karl E. Lapo[1,1], Anita Freundorfer[1,1], Tobias Linhardt[1,1], and Christoph K Thomas[1,1]

[1]University of Bayreuth

January 20, 2023

Abstract

During the morning transition, the nocturnal stable boundary layer, SBL, turns into the daytime convective boundary layer, making it an important phase for modelling and predicting temperature or pollutant distributions. By applying distributed temperature sensing suspended from a tethered balloon (0-200m height) and along a measurement tower (0-11m), for the first time we observed the detailed evolution of three complete morning transition phases with a high temporal (<10s) and spatial (<0.25m) resolution. Using distributed observations, the transition can be derived solely from a change in spatially continuous observations of static stability. It was validated that the transition occurs at the top and the bottom of the SBL simultaneously and advection of heat was identified as a main driver in addition to local surface warming. The transition is characterized by complex structures and small-scale variability, highlighting how distributed temperature sensing is a crucial tool for future research.

Manuscript submitted to Geophysical Research Letters (GRL)

Supporting Information for

A. M. Fritz[1], K. E. Lapo[1,2], A. Freundorfer[1], T. Linhardt[1], and C. K. Thomas[1,2]

[1]Micrometeorology Group, University of Bayreuth, Germany. [2]Bayreuth Center of Ecology and Environmental Research (BayCEER), University of Bayreuth, Germany.

Contents of this file

Text S1 to S3 Figure S1

Introduction

Text S1 provides additional detail on the corrections applied for the sonic anemometer data and on the definition of the morning transition. Text S2 gives technical details on the DTS deployments and calibration used during the LOVE19 field campaign (Lapo et al., 2020). Text S3 explains how the flying height of the tethered balloon and the height of each measurement along the fiber-optic cable were calculated. Figure S1 shows the outline of the stable boundary layer as observed by FlyFox on the 26 July 2019 and the two linear models used for the detection of the start time of the morning transition phase at the top of the stable boundary layer.

Text S1. Sonic Anemometers (CSAT).

Four sonic anemometers (CSAT3, Campbell scientific, Logan, UT, USA) were mounted along a measurement tower at heights of 0.5m, 1.25m, 4m, and 12m. The sampling frequency was 20Hz. Spikes in the data were removed according to Vickers & Mahrt (1997) using a window size of 300s, an initial spike criterion of 6.5 standard deviations and a maximum of 5 iterations. A cross-wind correction but no coordinate rotation and no correction for spectra losses was applied. The data was block averaged to 1min values. Temperature gradients were calculated between two adjoining sonic anemometers.

The morning transition was defined in two ways: as the point in time when the sensible heat flux changed to positive and as the point in time when the static stability changed to neutral or unstable. In both definitions, the MT was defined as the time from which the change in the observed variable was consistent meaning that 20 of the past 30 measurements did not fulfil the criterion while the upcoming 5 measurements and overall 25 of the upcoming 30 measurements did fulfil the criterion.

Text S2. DTS Calibration and setup

For FlyFox, a pair of twisted PVC fiber-optic cables was attached to a tethered balloon which was operated at 200m height. Every 0.254m along the fiber, air temperature was observed using a XT-DTS (Silixa, London, United Kingdom) in a single-ended configuration. Data consists of one 5s average every 10s. Four water baths were used as reference sections for calibration. Calibrated temperatures had a bias between 0.07K and 0.11K, which is acceptable given the length of fiber and power loss associated with the strain on the fiber. Data were processed using *pyfocs*(Lapo & Freundorfer, 2020).

The experiment was limited to calm days as the balloon was strongly influenced by horizontal wind speeds. An increase of these winds by$1\,\frac{m}{s}$ corresponded to a lowering of the balloon by 3m. Furthermore, the flights were legally restricted to 200m height and non-night time periods.

For the tower-DTS the fiber-optic cable was loosely buffered inside a high-resistance stainless steel sheath filled with gel and coated by 0.2 mm thick polyethylene (outer diameter 1.32 mm, Model C-Tube, Brugg, Switzerland). The calibration of the DTS was conducted using the explicit matrix inversion following Hausner et al. (2011). Calibrated temperatures have a bias of 0.3K which is relatively large, likely due to multiple different fiber types being observed in a single-ended configuration. Data were processed using *pyfocs* (Lapo & Freundorfer, 2020).

See Lapo et al. (2020) for additional data and experiment documentation.

Text S3. Calculation of Measurement Heights for FlyFox.

The height of the balloon and thus the conversion of the LAF-coordinate from the DTS device to height above the ground needed to be derived as it was not observed directly. Using the tether probe observations and the temperature profile from the DTS, an iterative approach was employed as multiple quantities had to be estimated simultaneously.

The flying height of the balloon was determined using the hypsometric equation

$$z = \frac{R * T_v}{g} * \ln\left(\frac{p_{\mathrm{sfc}}}{p(z)}\right) \qquad (1)$$

where z is height agl, R is the specific gas constant for dry air, T_v is the mean virtual temperature between the surface and z, p_{sfc} is the pressure measured at the surface, and $p(z)$ is the pressure at height z. Biases

in the tether probe pressure were removed by comparing the observations of the tether probe sensor and the surface sensor when the balloon was at the surface. Virtual temperatures T_v were calculated as

$$T_v\left(z\right) \approx T\left(z\right) * \left[1 + 0.61\ r_v\left(z\right)\right] \qquad (2)$$

with $r_v\left(z\right)$ being the mixing ratio of water vapor pressure.

Solving the hypsometric equation for height required an iterative solution, as T_v requires water vapor pressure, $r_v(z)$, which depends on $p(z)$. For step 1, the flying height h was estimated by replacingT_v in Equation 1 with the dry-bulb temperature from the DTS averaged between the surface, z_{sfc}, and the height of the balloon, h. For step 2, the height of each measurement along the fiber-optic cable was linearly interpolated between the surface and h. From this profile of T(z),$p(z)$ was estimated by solving Eq. 1 for the pressure at each measurement height, z.

For step 3, T_v was calculated which required saturated water vapor pressure, $e_s(z)$, relative humidity, $\Phi(z)$, and the mixing ratio of water vapor pressure, $r_v(z)$. Using the method recommended by the World Meteorological Organization (2018),$e_s(z)$ was derived as:

$$e_s\left(z\right) = 6.112 \exp\left(\frac{17.62 * T\left(z\right)}{243.12 + T\left(z\right)}\right). \qquad (3)$$

$\Phi(z)$ was linearly interpolated between the surface and the tether probe. For step 4, from these quantities, $r_v(z)$ was calculated as

$$r_v\left(z\right) = \frac{0.622 * \phi\left(z\right) * e_s\left(z\right)}{p\left(z\right) - \ \phi\left(z\right) * e_s\left(z\right)}. \qquad (4)$$

With $r_v(z)$, virtual temperatures were derived using Eq. 2 and used for an additional iterations of the algorithm. Only one iteration was needed as further iterations had a negligible effect on estimating$h$.

Finally, potential temperatures were computed as

$$\theta\left(z\right) = T\left(z\right) * \left(\frac{p_{\mathrm{sfc}}}{p\left(z\right)}\right)^{\frac{R}{c_p}} \qquad (5)$$

where R is the specific gas constant for dry air and c_p is the specific heat capacity. Virtual potential temperatures,θ_v, were computed using Equation 3 with T being replaces byθ.

The height of any individual observation along the fiber was linearly interpolated between the height of the fiber as it left the spool at the surface, z_{sfc}, and the top of the DTS transect, z_{top}, using step sizes,Δz, equal to the average height step size for the entire flight

$$\Delta z = \frac{z_{\mathrm{top}} - z_{\mathrm{sfc}}}{N_{\mathrm{LAF}}} \qquad (6)$$

where N_{LAF} is the number of DTS observations along the tethered fiber optic cable and the overbar denotes a time average. This step enables an equal-spaced vertical grid for the entire flight.

The approach for estimating the height of the balloon assumes regularly-spaced observations in height, i.e. a straight fiber. The fiber optic cable would bend away from the tether, as the tether carried more tension than the fiber optic cable. The deviation between the tether and the fiber optic cable was larger during

stronger winds. The balloon's height would most strongly respond to horizontal wind speed, descending as the wind speed increased. Other factors, specifically the vertical wind speed, had an order of magnitude smaller impact on the balloon height.

The linear assumption was evaluated against two non-linear models (parabolic and hyperbolic cosine functions) of the fiber's path. The parabolic function best modeled the distance between two measurements, the overall length of the fiber, and the horizontal offset between the tether and the fiber. However, the linear function was used for converting the length along the fiber to height as it was simpler to compute and had only a negligible effect on the derived temperature gradients. The linear model was found to perform well during calm conditions when the angle between the tether and vertical was less than 10°. During flights with stronger winds the balloon lowered enough (up to 15m) that the uncertainty in height from the linear model exceeded the uncertainty in balloon height introduced by the uncertainty in the tethersonde observations. However, the height uncertainty is at most 2.315m and decreases above a height of 15m as the linear model is least accurate near the surface. As a result, the linear height model was used for all observations due to its simplicity and relatively minor errors even for the strongest observed wind speeds. These height deviations had a negligible impact on the magnitude of the vertical potential temperature gradient, but did adjust the height of the gradient maximum.

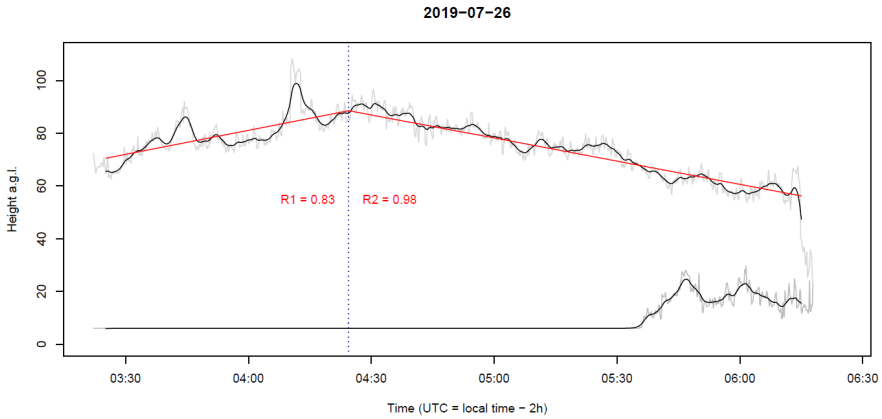

Figure S1. Detection of the start of the morning transition phase, MTP, at the top of the stable boundary layer, SBL, from the FlyFox data measured on the 26 July 2019. Grey line = detected SBL outline. Black line = low pass filtered SBL outline (1st order, wavelength threshold of 3min). Red line = fitted linear models. Dotted line = start of the MTP at the SBL top.

Hosted file

`essoar.10505541.2.docx` available at https://authorea.com/users/547529/articles/602773-revealing-the-evolution-and-small-scale-variability-of-the-morning-transition-phase-in-the-atmospheric-boundary-layer-using-distributed-temperature-sensing

Revealing the Evolution and Small-Scale Variability of the Morning Transition Phase in the atmospheric boundary layer using Distributed Temperature Sensing

A. M. Fritz[1], K. Lapo[1,2], A. Freundorfer[1], T. Linhardt[1], and C. K. Thomas[1,2]

[1]Micrometeorology Group, University of Bayreuth, Germany. [2]Bayreuth Center of Ecology and Environmental Research (BayCEER), University of Bayreuth, Germany.

Corresponding author: Christoph Thomas (christoph.thomas@uni-bayreuth.de)

Key Points:

- A novel technique, distributed temperature sensing below a tethered balloon, reveals the detailed evolution of the morning transition.
- A new definition of the transition is provided that better reflects the strong spatiotemporal variability of this process.
- The new technique enables the direct investigation of processes that normally must be neglected, providing an observational breakthrough.

Abstract

During the morning transition, the nocturnal stable boundary layer, SBL, turns into the daytime convective boundary layer, making it an important phase for modelling and predicting temperature or pollutant distributions. By applying distributed temperature sensing suspended from a tethered balloon (0-200m height) and along a measurement tower (0-11m), for the first time we observed the detailed evolution of three complete morning transition phases with a high temporal (<10s) and spatial (<0.25m) resolution. Using distributed observations, the transition can be derived solely from a change in spatially continuous observations of static stability. It was validated that the transition occurs at the top and the bottom of the SBL simultaneously and advection of heat was identified as a main driver in addition to local surface warming. The transition is characterized by complex structures and small-scale variability, highlighting how distributed temperature sensing is a crucial tool for future research.

Plain Language Summary

During the night a stable boundary layer, SBL, forms at the earth's surface which is characterized by cold air at the surface, increasing temperatures with height, and very little mixing. Its counterpart is the convective boundary layer, CBL, during the day which has the opposite characteristics. Both the SBL and the CBL are relatively well studied, however, the morning transition between the two is less well understood, degrading weather and air-quality forecasts.

To improve upon this, we measured air temperature below a tethered balloon during the morning transition using a technique called distributed temperature sensing. These measurements gave an unprecedented view of the morning transition. We developed a method for precisely detecting the detailed structure of the morning transition. The morning transition is a highly variable process which previously had been simplified due to data limitations. It starts simultaneously from above and at the surface, starts and stops while taking over an hour to occur, and is strongly influenced by wind direction. While more work using distributed temperature sensing is necessary to understand why the air takes so long to respond to the rising sun, we demonstrate how critical this technique is to future research.

1. Introduction

The mid-latitude atmospheric boundary layer, ABL, undergoes a diurnal cycle between a daytime convective boundary layer, CBL, and a nocturnal stable boundary layer, SBL. The transition from the SBL to the CBL is of interest for weather and air-quality forecasts as it significantly influences the distribution of temperature, humidity, or pollutants in the morning (e.g., Holtslag et al., 2013; Morbidelli et al., 2011). Nevertheless, it is difficult to understand since processes that are typically simplified or neglected become important, including advection, shear, and entrainment, (Angevine et al., 2020; Bange et al., 2007; Wildmann et al., 2015).

Numerous studies attempted to describe the SBL and its Morning Transition (MT) to the CBL using experiments and numeric models. Angevine et al. (2011) defined the MT by the times of sunrise, first sign change of sensible heat flux (crossover), and first statically unstable stratification across 200m height (onset). They found that the sensible heat flux, H, itself was too weak to drive the transition in the observed speed and hence emphasized the importance of entrainment from above. Lapworth (2006) similarly found a close relationship between crossover and a change in static stability. Further studies found that the entrainment from the Residual Layer, RL, into the SBL is shear driven (Beare, 2008) and that longwave radiative cooling of the SBL and the RL enhances the growth rate of the CBL (Edwards et al., 2014; Wildmann et al., 2015).

Previous studies mainly focused on flat terrain (Angevine et al., 2001; Basu et al., 2008; Higgins et al., 2018; Lapworth, 2006; Svensson et al., 2011). It was found that surface heterogeneity strongly modifies the diurnal cycle of the ABL and particularly the morning transition (Angevine et al., 2020; Holtslag et al., 2013; Wildmann et al., 2015). Hence, further studies on heterogeneous and mountainous terrain are needed to broaden our understanding of the MT.

Past experiments were conducted using point observations, remote sensing, or probes underneath a balloon or remotely-piloted aircraft. They were limited in vertical resolution and, consequently, relied on assumptions like stationarity or negligible advection that are commonly violated during the transition (Wildmann et al., 2015). Similarly, previous definitions of the transition did not allow for deriving any finer-scale structure. To get around these assumptions and to evaluate the detailed events of the transition, spatially continuous observations with a high temporal resolution are needed. These requirements can be fulfilled by Raman spectra distributed temperature sensing, DTS (Selker et al., 2006; Tyler et al., 2009). Along a fiber-optic cable, DTS enables high quality temperature measurements at a fine spatial ($\approx 0.12-0.5$m) and temporal resolution ($\approx 1-10$s). It has successfully been used to investigate the near-surface boundary layer (e.g., Krause et al., 2013; Thomas et al., 2012; Zeeman et al., 2014). Additionally, Higgins et al. (2018) and Keller et al. (2011) demonstrated its vertical applicability. Nevertheless, their experiments were limited in maximum flight height,

duration, and temporal resolution and hence were unable to use the full benefits of DTS to investigate boundary-layer processes.

Here, we demonstrate the observational breakthrough enabled by DTS on three mornings in July 2019. DTS was deployed below a tethered balloon (0-200m height) in a broad, mid-range mountain valley in south-east Germany. The static stability derived from these spatially continuous temperature observations gives detailed, novel insights into the behaviour of the SBL and the growth of the CBL during the transition. Using these unique data we define the Morning Transition Phase (MTP) from the first appearance of the CBL to the disappearance of the SBL. Here we use MT to refer to the general process of the transition and MTP to refer to this specific new definition. In addition to the balloon measurements, 4 sonic anemometers, DTS along a surface tower (0-11m height), and a ground-based radio-acoustic sounding system (SODAR-RASS) were used to investigate the transition.

Our study first compares the DTS measurements to those from the sonic anemometers to evaluate the consistency between the established MT detection based on the crossover and the new, stability-based MTP (Section 4.1). Then we analyze drivers of morning transition dynamics with a focus on entrainment at the SBL top (Section 4.2) and advection near the surface (Section 4.3). While these drivers were investigated before, the spatially continuous DTS observations of the entire SBL allow for their first direct observation and quantifying their effects.

2. Methodology

2.1. Experimental Site

In June and July 2019, the Large Eddy Observatory Voitsumra Experiment 2019 (LOVE19) took place in a broad, mid-range mountain valley in the Fichtelgebirge mountains, south-east Germany (50.0906N 11.8543E; 624m asl; Lapo et al., 2020). The valley is orientated from south-west to north-east with a main wind direction along the valley. The experimental site was located at a perennial extensive grassland in the flat valley bottom. All instruments were deployed within a maximum separation distance of 300m.

2.2. The Morning Transition (Phase)

Here, we define the MTP entirely based upon the change in static stability from stable to neutral or unstable, facilitating the unique spatiotemporal tracking of the MT from DTS. The MT studies mentioned in the introduction suffered from insufficient resolution to provide detailed structure of the MT. To distinguish between these two static stability regimes, a threshold of $0.04\frac{K}{m}$ for the vertical potential temperature gradient was used, with values exceeding it being statically stable and values below being a combined statically neutral or convective classification. This threshold is relatively large due to measurement uncertainty in the DTS data but provides consistency between the different

techniques and prevents non-physical temporal or spatial jumps in the SBL perimeter. For each instrument, the data collection and calculation of the transition is presented in the following subsections. Further details on the instrumental setup and calibration are provided in the supporting information (Texts S1, S2, S3).

2.2.1. Sonic anemometers

Four sonic anemometers (CSAT3, Campbell scientific, Logan, UT, USA) were placed along a measurement tower at heights of 0.5m, 1.25m, 4m, and 12m. Data were screened according to Vickers and Mahrt (1997) and block-averaged to 1min values. Turbulent fluxes were computed using the eddy covariance technique with a perturbation time scale of 1min. Temperature gradients were calculated between two adjoining sensors. Two point-based definitions for the onset of MT were tested: first by the sign change of H to positive and second by the static stability change to neutral or unstable.

2.2.2. DTS at the measurement tower (Tower-DTS)

Fiber-optic cables were deployed along a tower between 0.6m and 10.8m height. Air temperature was measured with a DTS instrument (Ultima-S 5km variant, Silixa, Elstree, United Kingdom) with 1s and 0.127m sampling resolution. In post-processing, data were further aggregated to 10s averages to reduce the influence of instrument noise.

DTS measured air temperature, T. From this quantity, static stability was estimated using vertical gradients, $\frac{\partial T}{\partial z}$. These gradients were derived using rolling block averages with a window size of $\Delta z = 1.29\,m$ (Equation 1). Different calculation methods and window sizes were tested, but the chosen method had a desired trade-off between sharpness of gradients and reducing the effects of measurement uncertainty. $\frac{\partial T}{\partial z}(z)$ was estimated by

$$\frac{\partial T}{\partial z}(z) = ¿\partial T[z, z+\Delta z]> - ¿\partial T[z-\Delta z, z]> \frac{¿}{\Delta z} (1) ¿$$

where <> indicates spatial averaging.

Stable ($\frac{\partial T}{\partial z} \geq 0.04\,\frac{K}{m}$) and non-stable ($\frac{\partial T}{\partial z} < 0.04\,\frac{K}{m}$) layers were identified. Layers with a duration of less than 60 s were disregarded and included in the surrounding layer. The SBL was defined as the extent of all stable layers either connected to the largest nocturnal stable layer or located at the top or bottom of the profile. The MTP starts with the first appearance of the CBL and ends with the completed disappearance of the SBL, as observed at all levels of the Tower-DTS.

2.2.3. Flying Fiber-Optics Experiment (FlyFox)

For FlyFox a fiber-optic cable was attached to a tethered balloon at 200m height. Air temperature was observed using a DTS instrument (XT, Silixa, London, United Kingdom) with a 10s temporal and 0.254m spatial resolution. Immediately below the balloon, a tethersonde was deployed to observe pressure and relative humidity at a resolution of 1s (BME280, Bosch sensortec GmbH, Reutlingen, Germany).

Determining the flying height of the balloon is explained in detail in the supporting information (Text S3). The height of each measurement section along the fiber-optic cable was approximated linearly between the surface and the balloon's height.

Similar to the Tower-DTS data, temperature gradients were calculated using Equation 1. Due to the greater vertical extent of the measurement and the larger scales of the features observed at heights greater than those of the Tower-DTS, Δz was set to 4m. The definition of the SBL follows the same procedure as for the Tower-DTS (Section 2.2.2). Here, due to the difference in scales, a minimum duration of 10min is required for a layer to be considered. Additionally, the outer boundary of the SBL was smoothed by a low pass filter (1st order, wavelength threshold of 3min) to highlight the relevant, larger scales.

The MTP has a separate start time for the bottom and the top of the SBL. The bottom-start occurs when the SBL desolves from the surface, i.e. in 6.1m height due to data availability and calculation of gradients (Equation 1). The top-start was derived from a segmented regression to the upper boundary of the SBL. The breakpoint of the segmented regression was varied in time and height and the breakpoint of the model combination with the largest mean R^2 for both models determined the top-start of the MTP as it indicates a trend change at the SBL top (Figure S1). The slope of the linear model used during the MTP additionally quantifies the entrainment velocity at the boundary layer top directly. The end of the MTP is reached once the entire profile is neutrally or unstably stratified.

2.2.4.SODAR-RASS

A SODAR-RASS (Model DSDPA90.64 and 1.29GHz RASS, Metek GmbH, Elmshorn, Germany) measured wind speed, wind direction, and air temperature averaged over 10min at a 20m vertical resolution between 30m and ~300m height. Temperature gradients were calculated from two adjoining gates.

The SBL was defined as the layer characterized by statically stable stratification and a direct connection to the dominant nocturnal stable layer near the surface. The MTP starts when the SBL height permanently falls below its mean nocturnal height (00:00 to 05:00; all times in UTC) and ends once the profile is neutrally or unstably stratified.

2.3. Ancillary observations

Net radiation was observed at 2m height by a 4-compoment radiometer (aspirated CNR-4, Kipp&Zonen, Delft, The Netherlands). A ceilometer (CHM 8k, Lufft Mess- und Regeltechnik GmbH,

Fellbach, Germany) measured cloud cover and cloud base heights at a 1min temporal and 5m spatial resolution. A PVC fiber-optic cable was deployed in a wide rectangle at approximately 1m height around the measurement tower to observe air temperature using the same calibration applied to the Tower-DTS and FLyFOX. It was used to quantify the horizontal temperature variability as the deviation from the spatial mean. These data were combined with the data from the sonic anemometers to estimate horizontal advection of sensible heat according to Moderow et al. (2007).

3. Results

The three mornings (22, 23, 26 July 2019; Figures 1, 2, 3, respectively) were characterized by weak winds ($\leq 2\frac{m}{s}$) within the lowest 150m and a high relative humidity before sunrise (≥ 90%), but no precipitation or fog. Winds above the SBL were predominantly easterly while within the SBL they varied between south (22, 23 July) and north (26 July; Figures 1a, 2a, 3a). Near the surface, wind directions showed stronger variability across the three MT. All days had predominantly cold-air advection towards the measurement tower at 1m height.

A time delay of about 40min was observed between the downwelling shortwave radiation, Rswd, exceeding 40W/m^2 at the net radiometer location and the sun reaching the FlyFox launch site which was caused by the shading of the nearby trees at low sun angles. The 150m long horizontal DTS transect showed a strong heterogeneity in temperature with differences of up to 3.1K and spatial standard deviations between $\pm 0.21 K$ and $\pm 0.32 K$ (Figure 1f, 2f, 3f). Before the start of the MTP, intense but small-scale heterogeneity was observed on all days indicative of submeso-scale motions (Pfister et al., 2019). With MTP commencement, the submeso-scale temperature structures disappeared, giving way to a larger scale temperature gradient across the field with colder temperatures near the FlyFox launch site and warmer temperatures to the north, especially on the sunnier days (23, 26 July). After the MTP, the large-scale temperature gradient largely dissolved into small-scale temperature perturbations indicative of CBL mixing.

3.1. 22 July 2019

The cloudiest morning had cloud covers between $\frac{5}{8}$ and $\frac{7}{8}$. Shortly before the flight, surface observations showed meandering winds between south and west. In addition, between 03:50 and 04:40, the sonic anemometers detected non-synchronous changes of wind directions between the 1.25m and 12m height with a mean direction change of 39° (±20°).

Near the surface, the sonic anemometers revealed an earlier stability change (dots) than crossover (triangles; Figure 1d) with a time delay of about 20min. The MTP from the Tower-DTS data started

even earlier at 04:08 (black line, Figure 1c). This start co-occurred with Rswd exceeding $40\frac{W}{m^2}$ but did not begin at the bottom of the profile but 3.2m to 6.0m height. Between 1.9m and 3.2m the stratification remained stable for an additional 15min. From 04:11 until 04:51, the SBL boundary showed a distinct up and

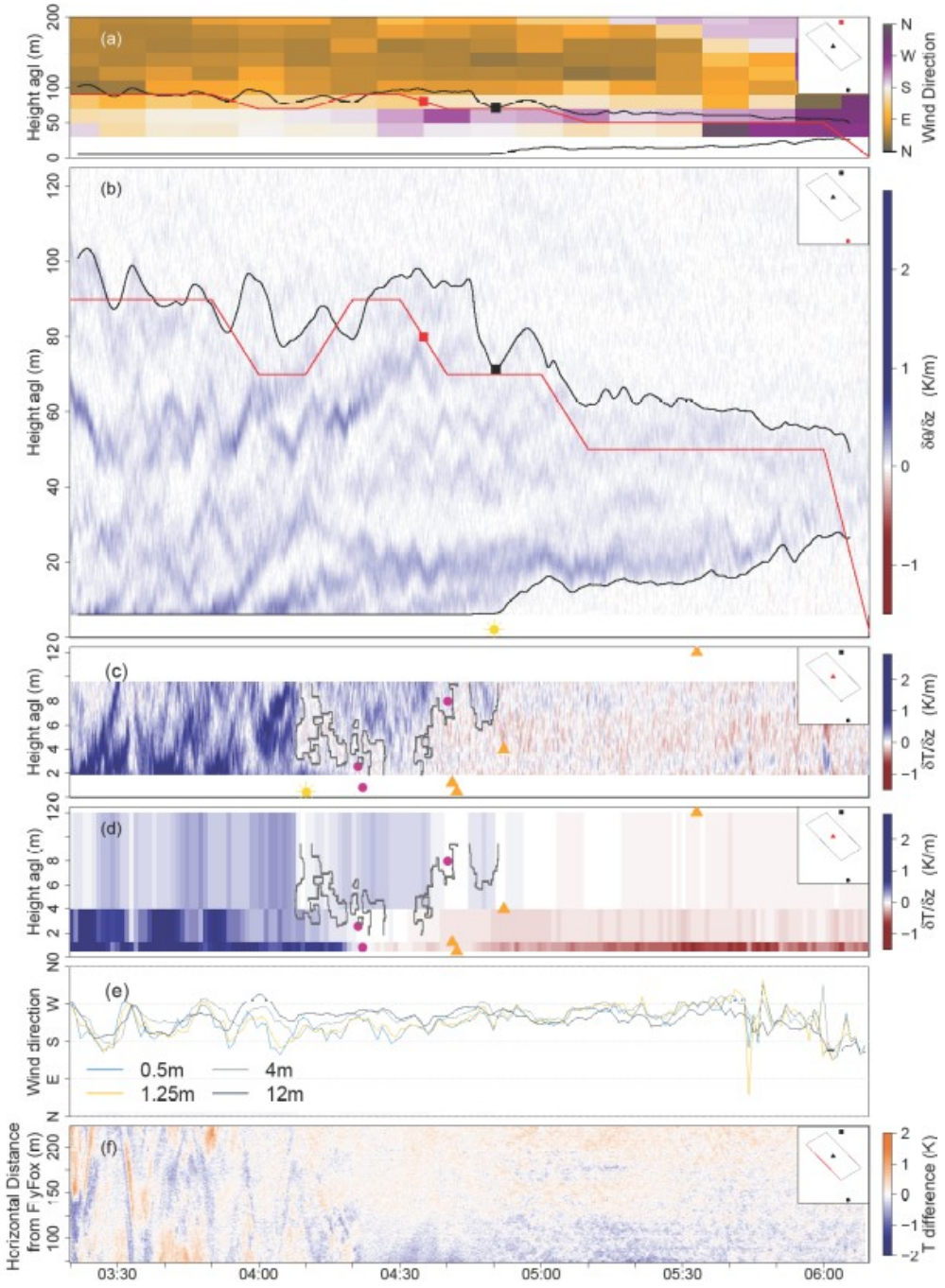

Figure 1. 22 July 2019.

(a) Wind directions measured by SODAR-RASS. Black line = SBL outline from FlyFox. Orange line = SBL outline from SODAR-RASS. Squares = MTP start derived from the corresponding SBL outline. **(b)** Temperature gradients derived from FlyFox. Lines and squares as in (a). Sun = first time the sun hit the surface right below FlyFox. Note the change on the y-axis scale between (a) and (b).

(c) Temperature gradients derived from Tower-DTS. Black line = SBL outline from Tower-DTS. Purple dots = MT from sonic anemometer stability change. Brown triangles = MT from crossover observed by sonic anemometers. Sun = first time the Rswd exceeded $40\,\frac{W}{m^2}$ at the net radiometer.
(d) Temperature gradients derived from sonic anemometers. Other symbols as in (c).
(e) Wind directions measured by sonic anemometers.
(f) Temperature deviation of the horizontal DTS from the spatial mean.
Note that all subplots include an inset map showing the relative position of all observations with the displayed observation's location in red.

down movement found in both the sonic anemometer and Tower-DTS observations (Figure 1c, d).

Further aloft, FlyFox and the SODAR-RASS detected a MTP with a duration of 78min (FlyFox) and 90min (SODAR-RASS; Figure 1b) and a similar end. FlyFox observed an entrainment velocity of $-0.0068\,\frac{m}{s}$ and a wind direction change of $58° \pm 24°$ at the SBL top (Figure 1a). In addition to the evolution of the upper SBL boundary, FlyFox observed the growth of the CBL below which was remarkably slow compared to the other days (Figures 2b, 3b). This growth started simultaneously with the SBL starting to dissolve from above and the sunlight reaching the launching area.

3.2. 23 July 2019

Cloud cover was least ranging between $\frac{1}{8}$ and $\frac{2}{8}$ and correspondingly the influence of the nearby trees on the horizontal temperature differences was large by casting shadows (Figure 2f). The sonic anemometers yielded similar results for the tested definitions for transition onset (Figure 2d). Unlike in greater heights, the stability change between 0.5m and 1.25m height did not occur between the crossovers observed by the adjoining sonic anemometers, but 25min and 27min earlier. In the Tower-DTS data, the first unstable layers arose at 04:05 but the main transition started at 04:24 between 3.2 and 4.5m and at 04:28 from 1.9m (Figure 2c).

Further aloft, FlyFox revealed an MTP duration of 78min with an entrainment velocity of $-0.0072\,\frac{m}{s}$ and a wind direction change of $40° \pm 32°$ at the SBL top (Figure 2a). The transition began at the top (04:39) before the stability first changed at the bottom (04:56; Figure 2b). The start of the transition at the surface occurred shortly after the sun reached the launching area. The SODAR-RASS only observed the changes at the top of the SBL. Here, the MTP started 6min later than in the FlyFox data and ended at the same time.

3.3. 26 July 2019

229 On this day, cloud cover was intermediate between $\frac{2}{8}$ and $\frac{5}{8}$. Near the surface, winds were especially

230 calm between 05:00 and 06:00 (¿$0.6\,\frac{m}{s}$) and wind directions changed rapidly (Figure 3e). The sonic
231 anemometer at 12m height observed strong directional changes unsynchronized with the lower three
232 instruments. After 06:00, wind speeds increased rapidly (not shown) and winds became predominantly
233 north-easterly.

234 All observational systems near the surface yielded a similar start of the MTP (Figure 3c, d). The
235 results based on the crossover yielded the fastest MTP of only 30min. In contrast, the Tower-DTS
236 detected the slowest MTP (62min) which started with a fast growth of the CBL at 04:51 up to about
237 6.5m but then revealed strongly varying stability conditions within the entire profile (Figure 3c). These
238 varying temperature gradients inhibited a precise detection of the CBL.

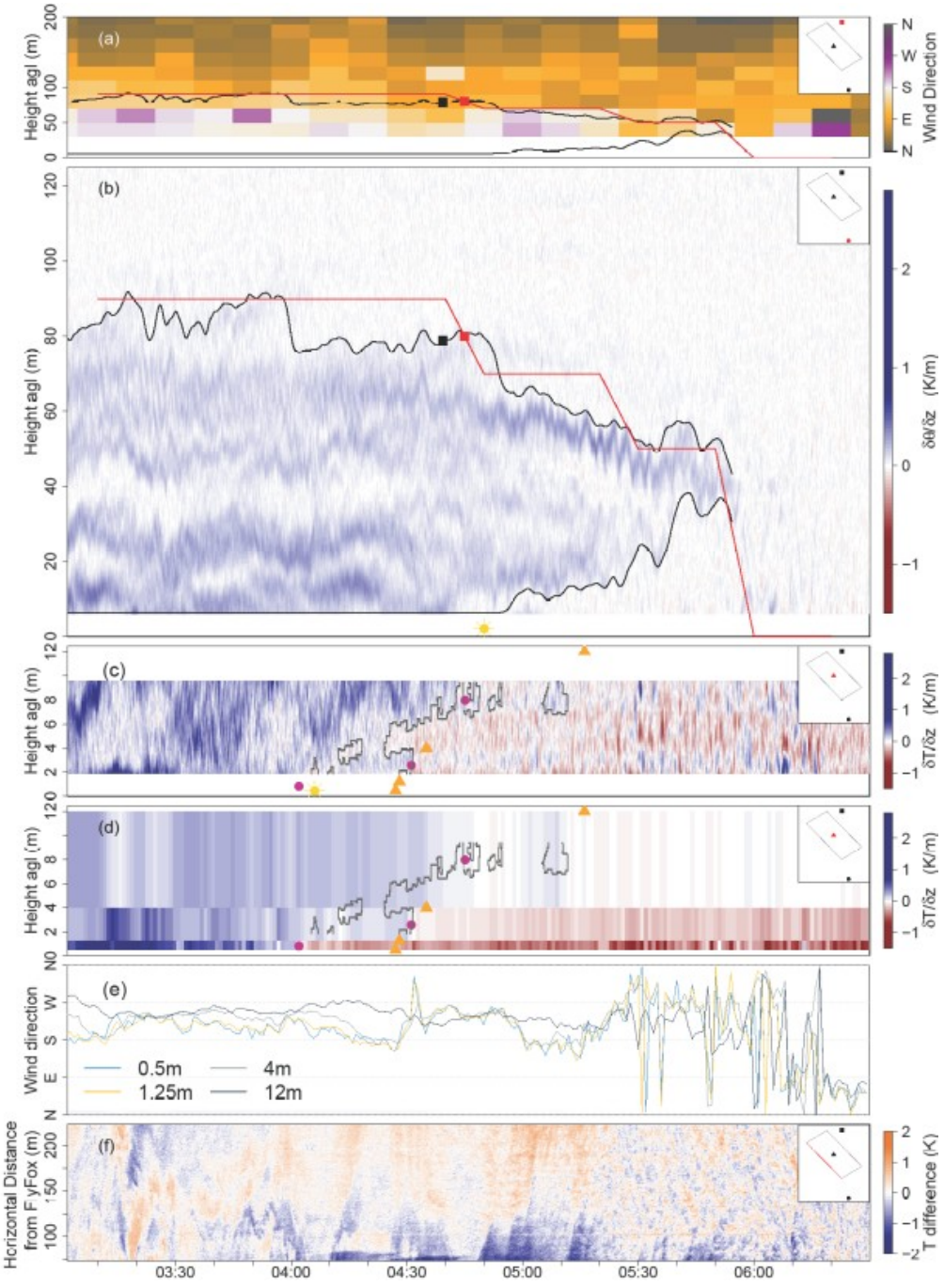

Figure 2. As in Figure 1 but for 23 July 2019.

At the top of the SBL, FlyFox observed a long transition (113min) and correspondingly a small entrainment velocity ($-0.0049 \frac{m}{s}$¿. Additionally, the wind direction change at the SBL top was smaller than on the other two days ($21° \pm 12°$). From FlyFox, the transition at the top started 71min earlier than the transition at the bottom and 39min earlier than the transition observed by the SODAR-RASS. Near the surface, the FlyFox MTP occurred approximately 30min after the sun reached the launching area which was remarkably different compared to the other days.

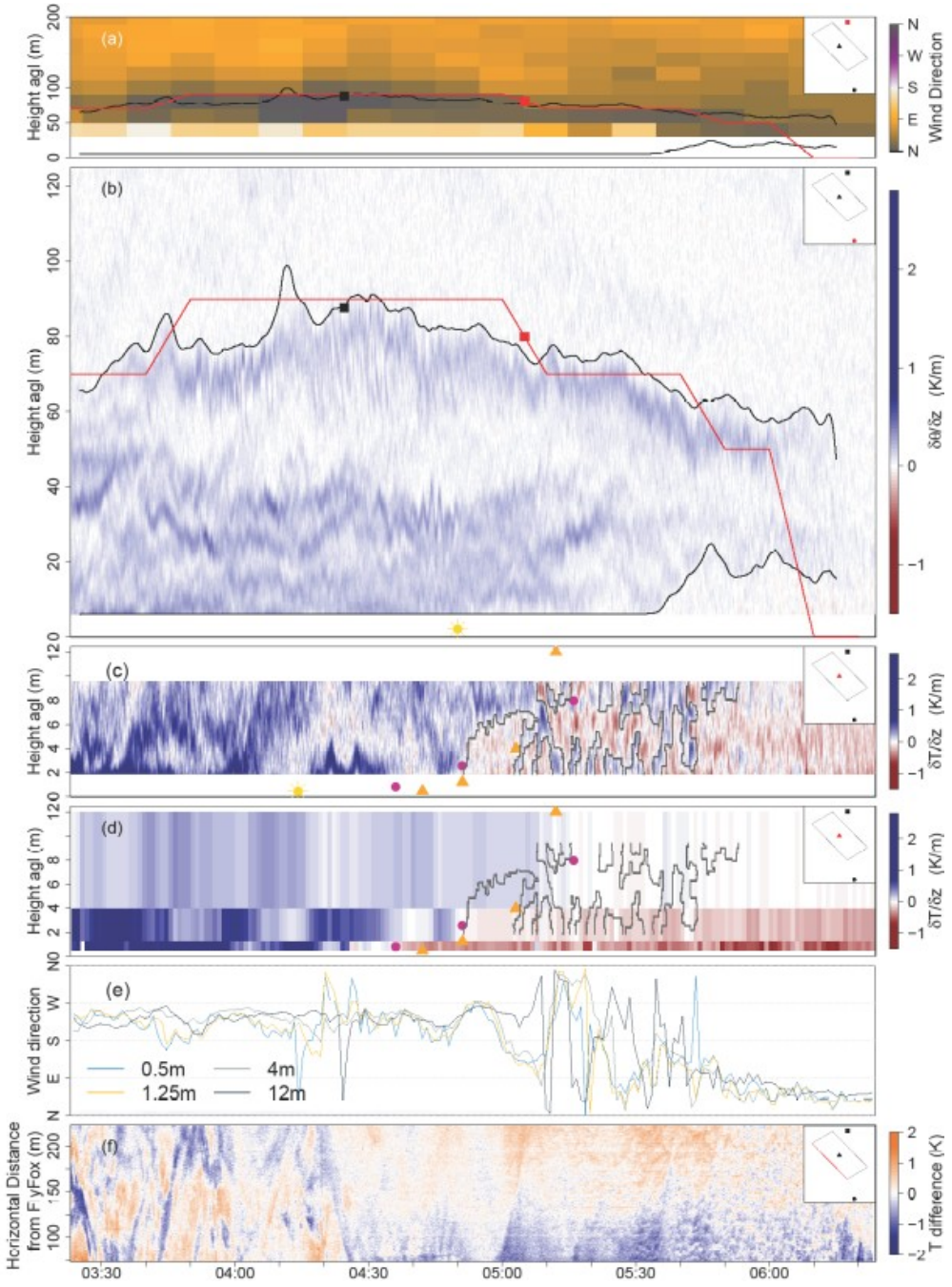

Figure 3. As in Figure 1 but for 26 July 2019.

4. Discussion

4.1. Comparing transition detection methods

In previous MT research, the beginning of the transition was defined from H near the surface while its end was determined from the static stability across the lowest 200m height (e.g., Angevine et al., 2001; Beare, 2008). In contrast, our flux-tower observations (0.5m to 12m) demonstrate a discrepancy between the H- and stability-based definitions. On 22 July, the stability change preceded the crossover in the sign of H by 20min (Figure 1d). On the other days, neither a constant delay nor a defined order of the events was observed (Figure 2d, 3d). The discrepancy likely results from the threshold chosen

for the stability-based definition ($0.04\frac{K}{m}$) and the exact height at which observations are made or computed for: the crossover is calculated at the exact height of each sonic anemometer, while the stability change is calculated for the height interval between two sonic anemometers. Therefore, we propose to define the MTP solely from the change in static stability as it provides consistency in the detection of the start and end of the transition.

Furthermore, the stability-based definition offers the advantage of being applicable to spatially-distributed systems such as DTS. For a stability-based definition, the flux-tower and the Tower-DTS observations agree after considering their different height intervals, Δz. The stability changes computed for the sonic anemometers represent Δz of 0.75m, 2.75m, and 8m height while each DTS stability change represents a Δz of 2.57m. The stability change between the 1.25m and 4m sonic anemometers ($\Delta z = 2.75 m$) always occurred simultaneously with the stability change between 1.40m and 3.97m for the DTS data ($\Delta z = 2.57 m$; Figure 1c, 2c, 3c). Furthermore, on 22 July, the DTS observed an isolated stable layer (4:11 to 4:51; Figure 1c) which was large enough to additionally appear in the sonic anemometer data (Figure 1d). However, the sonic anemometers were unable to detect the fine spatial structure observed by the DTS, especially under rapidly changing stability conditions as observed on 26 July (05:02 to 05:53; Figure 3c).

The high-resolution DTS observations revealed that the MTP is a much more complex process than a one-directional rise of the CBL eroding the SBL. It can start over several meters simultaneously (3.2m to 6.0m; Figure 1c) or independently at different heights, separated by intervening stably stratified air (1.9m and 4.0m; Figure 2c). Furthermore, the growth of the CBL can be interrupted (6.5m; 04:54 to 05:08; Figure 3c), stable layers can re-emerge and intersperse the already convective layer with stably stratified air (Figure 3c). These processes make a differentiation between the SBL and CBL non-trivial during the MTP, especially with point observations, thereby demonstrating the need for spatially continuous observations. However, such details are hidden without the continuous and fine-resolving DTS.

FlyFox observed many different temporal and spatial scales which characterize the MT (Angevine et al., 2020; Van Driel and Jonker, 2011) and revealed for the first time the entire evolution of the MTP. Within the SBL, FlyFox observed rapidly evolving structures of stably and neutrally stratified air layers stacked on top of each other (e.g., 03:20 – 04:40; Figure 1b). Furthermore, during the MTP, FlyFox detected a lowering of the SBL top as well as a rise of the SBL bottom. The SODAR-RASS missed the transition at the bottom because of its relatively coarse vertical resolution and an elevated lowest gate, which was unable to resolve temperature gradients below 50m height. On 22 and 23 July, both measurements agreed well on the MTP duration (Figure 1b, 2b), while on 26 July the SODAR-RASS detected a much shorter transition (Figure 3b). The discrepancy on 26 July is not surprising as

the lack of spatial resolution in the SODAR-RASS data inhibits the detection of the slow decrease of the SBL top.

4.2. SBL depth and factors controlling the MTP at the SBL top

The influence of the surrounding mountains was reflected in the depth of the SBL. Likely as a result of cold-air drainage from the mountain slopes and subsequent cold-air pooling around the experimental site in the valley bottom, the SBL depth of 90m observed by FlyFox and the SODAR-RASS was larger than observed at other sites (e.g., Higgins et al., 2018; Keller et al., 2011).

Previous experiments showed that H is insufficient to drive the MT. This finding led to the conclusion that entrainment at the SBL top may be an additional driver without having direct observational evidence to support this claim (Angevine et al., 2001; Lapworth, 2006). Using the stability-inferred height of the SBL top, we can now derive and quantify the entrainment velocity at the SBL top directly, providing an observational break-through.

We exclude wind speed shear as the physical mechanism causing entrainment, in contrast to previous studies which could not directly observe the MTP (Angevine et al., 2001; Beare, 2008; Lapworth, 2006). The SODAR-RASS revealed that wind speed shear near the SBL top was small ($0\,\frac{m}{s}$ to $0.5\,\frac{m}{s}$). Additionally, these wind speed differences did not change with the MTP onset. However, all three days showed significant directional shear between the SBL and the RL (Figures 1a, 2a, 3a). The day with the longest MTP and smallest entrainment velocity (26 July) showed the smallest wind direction change and a different wind direction within the SBL than the days with the shorter MTPs. Therefore, we conclude that the wind direction change at the SBL top and the source regions of the advected air had a greater impact on the entrainment and the MTP than wind shear for this site, although further investigation with DTS is required to generalize these statements.

4.3. Factors controlling the MTP at the SBL bottom

Near the surface, the lowest FlyFox gradient was at 6.1m height causing an overlap of 4.2m with the Tower-DTS gradients. Despite this overlap, FlyFox and Tower-DTS observations revealed different transition dynamics, most likely due to the horizontal separation distance (160m). The horizontal DTS observations (Figure 1f, 2f, 3f) explicitly demonstrated the horizontal heterogeneity in air temperatures, the influence of shading during sunrise, and the evolution of different volumes of air. When combining its observations with those from the sonic anemometers, the influence of horizontal heat advection on the MTP was quantified. Starting shortly before the MTP on 22 July (03:50 to 04:30), the lower two sonic anemometers observed southerly winds while the upper two instruments observed more westerly winds (Figure 1e). The horizontal DTS revealed colder temperatures in the south than in the west which indicates that advection may have initiated this stability change between 3.2m and 6.0m height. Additionally, between 05:00 and 05:50 on 26 July, the wind directions varied

substantially and rapidly particularly at 12m height (Figure 3e). Both the period and signal correspond with rapidly changing stability conditions (Figure 3c) and strong horizontal temperature gradients (Figure 3f), underlining the influence of the different source regions of the advected air on the evolution of the MTP.

While the influence of horizontal heterogeneity and advection was considered previously (Angevine et al., 2020; Bange et al., 2007), it could not be observed directly to date. Since point observations can neither detect nor quantify advection, previous studies employed temporal averaging over longer periods to eliminate the influence of advection, which only then allowed for neglecting this potentially important process for interpretation (Angevine et al., 2001, 2020). In contrast, the combination of vertical and horizontal DTS observations presented here allowed for explicit detection and quantification of advection and the spatiotemporal variability of the near-surface airflow for the first time. This observational breakthrough eliminates the need for temporal averaging and allows for investigation of regions with systematic advection.

5. Conclusion

By deploying fiber-optic distributed temperature sensing (DTS) below a tethered balloon and along a measurement tower, the detailed evolution of the SBL and the growing CBL was observed. We showed that the SBL-CBL boundary can be derived continuously from changes in static stability. This detection of the SBL provides a good definition of the transition from the first appearance of the CBL to the complete disappearance of the SBL. From this we define the more physically meaningful morning transition phase. Our choice of solely using static stability across a larger vertical extent at fine resolution eliminates the inconsistencies between defining the beginning of the MTP from the sensible heat flux and the end from the static stability in previous studies.

Using this novel technique, we observed the small-scale variability of three complete morning transitions for the first time. Near the surface, the transition was found to start at different heights independently or simultaneously and to vary greatly even within small separation distances due to horizontal temperature heterogeneity and shading effects of surface topography and cover. Advection was determined as one of the main drivers and can now be investigated directly from the spatially continuous DTS data. Our study confirmed that the morning transition occurs simultaneously at the upper and lower boundary of the SBL and enabled the first direct measurements of the entrainment velocity at the SBL top. This works demonstrates the observational breakthrough enabled by DTS, making it a critical tool for future experiments.

6. Acknowledgements

This project has received funding from the European Research Council (ERC) under the European Union's Horizon 2020 research and innovation programme (grant agreement no. 724629 DarkMix).

All data described in this manuscript are accessible through the DOI 10.5281/zenodo.4312976.

7. Bibliography

Angevine, W. M., Baltink, H. K., & Bosveld, F. C. (2001). Observations of the morning transition of the convective boundary layer. *Boundary-Layer Meteorology*, *101*(2), 209–227. https://doi.org/10.1023/A:1019264716195

Angevine, W. M., Edwards, J. M., Lothon, M., LeMone, M. A., & Osborne, S. R. (2020). Transition Periods in the Diurnally-Varying Atmospheric Boundary Layer Over Land. *Boundary-Layer Meteorology*. https://doi.org/10.1007/s10546-020-00515-y

Bange, J., Spieß, T., & van den Kroonenberg, A. (2007). Characteristics of the early-morning shallow convective boundary layer from Helipod Flights during STINHO-2. *Theoretical and Applied Climatology*, *90*(1–2), 113–126. https://doi.org/10.1007/s00704-006-0272-2

Basu, S., Vinuesa, J. F., & Swift, A. (2008). Dynamic LES modeling of a diurnal cycle. *Journal of Applied Meteorology and Climatology*, *47*(4), 1156–1174. https://doi.org/10.1175/2007JAMC1677.1

Beare, R. J. (2008). The role of shear in the morning transition boundary layer. *Boundary-Layer Meteorology*, *129*(3), 395–410. https://doi.org/10.1007/s10546-008-9324-8

Edwards, J. M., Basu, S., Bosveld, F. C., & Holtslag, A. A. M. (2014). The Impact of Radiation on the GABLS3 Large-Eddy Simulation through the Night and during the Morning Transition. *Boundary-Layer Meteorology*, *152*(2), 189–211. https://doi.org/10.1007/s10546-013-9895-x

Goroch, A., Burk, S., & Davidson, K. L. (1980). Stability effects on aerosol size and height distributions. *Tellus*, *32*(3), 245–250. https://doi.org/10.3402/tellusa.v32i3.10579

Hausner, M. B., Suárez, F., Glander, K. E., van de Giesen, N., Selker, J. S., & Tyler, S. W. (2011). Calibrating single-ended fiber-optic raman spectra distributed temperature sensing data. *Sensors*, *11*(11), 10859–10879. https://doi.org/10.3390/s111110859

Higgins, C. W., Wing, M. G., Kelley, J., Sayde, C., Burnett, J., & Holmes, H. A. (2018). A high resolution measurement of the morning ABL transition using distributed temperature sensing and an unmanned aircraft system. *Environmental Fluid Mechanics*, *18*(3), 683–693. https://doi.org/10.1007/s10652-017-9569-1

Holtslag, A. A. M., Svensson, G., Baas, P., Basu, S., Beare, B., Beljaars, A. C. M., Bosveld, F. C., Cuxart, J., Lindvall, J., Steeneveld, G. J., Tjernström, M., & Van De Wiel, B. J. H. (2013). Stable atmospheric boundary layers and diurnal cycles: Challenges for weather and climate models. *Bulletin of the American Meteorological Society*, *94*(11), 1691–1706. https://doi.org/10.1175/BAMS-D-11-00187.1

Keller, C. A., Huwald, H., Vollmer, M. K., Wenger, A., Hill, M., Parlange, M. B., & Reimann, S. (2011). Fiber optic distributed temperature sensing for the determination of the nocturnal atmospheric boundary layer height. *Atmospheric Measurement Techniques*. https://doi.org/10.5194/amt-4-143-2011

Krause, S., Taylor, S. L., Weatherill, J., Haffenden, A., Levy, A., Cassidy, N. J., & Thomas, P. A. (2013). Fibre-optic distributed temperature sensing for characterizing the impacts of vegetation coverage on thermal patterns in woodlands. *Ecohydrology*, *6*(5), 754–764. https://doi.org/10.1002/eco.1296

Lapo, K., & Freundorfer, A. (2020). *klapo/pyfocs v0.5*. https://doi.org/10.5281/ZENODO.4292491

Lapo, K., Freundorfer, A., Fritz, A., Schneider, J., Olesch, J., Babel, W., & Thomas, C. K. (2020). *Large-eddy Observatory, Voitsumra Experiment 2019 (LOVE19)*. https://doi.org/10.5281/ZENODO.4312976

Lapworth, A. (2006). The morning transition of the nocturnal boundary layer. *Boundary-Layer Meteorology*, *119*(3), 501–526. https://doi.org/10.1007/s10546-005-9046-0

Moderow, U., Feigenwinter, C., & Bernhofer, C. (2007). Estimating the components of the sensible heat budget of a tall forest canopy in complex terrain. *Boundary-Layer Meteorology*, *123*(1), 99–120. https://doi.org/10.1007/s10546-006-9136-7

Morbidelli, R., Corradini, C., Saltalippi, C., & Flammini, A. (2011). Atmospheric stability and meteorological scenarios as inputs to air pollution transport modeling. *Water, Air, and Soil Pollution*, *218*(1–4), 275–281. https://doi.org/10.1007/s11270-010-0640-5

Pfister, L., Lapo, K., Sayde, C., Selker, J., Mahrt, L., & Thomas, C. K. (2019). Classifying the nocturnal atmospheric boundary layer into temperature and flow regimes. *Quarterly Journal of the Royal Meteorological Society*, *145*(721), 1515–1534. https://doi.org/10.1002/qj.3508

Selker, J., van de Giesen, N. C., Westhoff, M., Luxemburg, W., & Parlange, M. B. (2006). Fiber optics opens window on stream dynamics. *Geophysical Research Letters*, *33*(24), 27–30. https://doi.org/10.1029/2006GL027979

Svensson, G., Holtslag, A. A. M., Kumar, V., Mauritsen, T., Steeneveld, G. J., Angevine, W. M., Bazile, E., Beljaars, A., de Bruijn, E. I. F., Cheng, A., Conangla, L., Cuxart, J., Ek, M., Falk, M. J., Freedman, F., Kitagawa, H., Larson, V. E., Lock, A., Mailhot, J., … Zampieri, M. (2011). Evaluation of the diurnal cycle in the Atmospheric Boundary Layer over land as Represented by a Variety of Single-Column models: The second GABLS EXperiment. *Boundary-Layer Meteorology*, *140*(2), 177–206. https://doi.org/10.1007/s10546-011-9611-7

Thomas, C. K., Kennedy, A. M., Selker, J. S., Moretti, A., Schroth, M. H., Smoot, A. R., Tufillaro, N. B., & Zeeman, M. J. (2012). High-Resolution Fibre-Optic Temperature Sensing: A New Tool to Study the Two-Dimensional Structure of Atmospheric Surface-Layer Flow. *Boundary-Layer Meteorology*, *142*(2), 177–192. https://doi.org/10.1007/s10546-011-9672-7

Tyler, S. W., Selker, J. S., Hausner, M. B., Hatch, C. E., Torgersen, T., Thodal, C. E., & Schladow, S. G. (2009). Environmental temperature sensing using Raman spectra DTS fiber-optic methods. *Water Resources Research*, *46*(4), 1–11. https://doi.org/10.1029/2008WR007052

Vickers, D., & Mahrt, L. (1997). Quality control and flux sampling problems for tower and aircraft data. *Journal of Atmospheric and Oceanic Technology*, *14*(3), 512–526. https://doi.org/10.1175/1520-0426(1997)014<0512:QCAFSP>2.0.CO;2

Wildmann, N., Rau, G. A., & Bange, J. (2015). Observations of the Early Morning Boundary-Layer Transition with Small Remotely-Piloted Aircraft. *Boundary-Layer Meteorology*, *157*(3), 345–373. https://doi.org/10.1007/s10546-015-0059-z

World Meteorological Organization. (2018). *Guide to Instruments and Methods of Observation: Vol. I* (2018th ed., Issue 8). https://library.wmo.int/index.php?lvl=notice_display&id=12407

Zeeman, M. J., Selker, J. S., & Thomas, C. K. (2014). Near-Surface Motion in the Nocturnal, Stable Boundary Layer Observed with Fibre-Optic Distributed Temperature Sensing. *Boundary-Layer Meteorology*, *154*(2), 189–205. https://doi.org/10.1007/s10546-014-9972-9